


Nonlinear self-sustaining dynamics in cavity magnomechanicsWenlin Li ^{1,*}, Jiong Cheng,^{2,3} Wei-jiang Gong,¹ and Jie Li²¹College of Sciences, Northeastern University, Shenyang 110819, China²Interdisciplinary Center of Quantum Information, State Key Laboratory of Modern Optical Instrumentation and Zhejiang Province Key Laboratory of Quantum Technology and Device, Department of Physics, Zhejiang University, Hangzhou 310027, China³Department of Physics, School of Physical Science and Technology, Ningbo University, Ningbo 315211, China

(Received 8 May 2023; revised 7 August 2023; accepted 8 September 2023; published 25 September 2023)

A recent experiment [R. C. Shen *et al.*, *Phys. Rev. Lett.* **129**, 123601 (2022)] has demonstrated the occurrence of nonlinearity-induced asymptotic bistability in cavity magnomechanics. As an extension, we explore the theoretical ground of diverse potential self-sustaining effects in cavity magnomechanics by analyzing its nonlinear dynamics. The attractors which suggest dynamical multistability for the limit cycles are mapped out to the parameter space by deriving the corresponding slow amplitude dynamics. Our quantitative analysis also includes the fluctuation-dissipation process, which quantitatively predicts non-Gaussian phase spreading, amplitude squeezing, and the mixture of multiple limit cycle states. We finally explore the quantum self-sustaining dynamics by solving the full quantum master equation. The paper lays the foundation for various applications, e.g., high-precision measurements, squeezed-state and non-Gaussian-state preparation, and nonlinearly induced quantum phase transitions, based on cavity magnomechanics.

DOI: [10.1103/PhysRevA.108.033518](https://doi.org/10.1103/PhysRevA.108.033518)**I. INTRODUCTION**

It has been recently revealed that in ferromagnetic systems, especially in yttrium iron garnet (YIG), the quanta of collective excitations of a spin ensemble can be used to realize strong light-matter interactions so that the corresponding Kittel mode can strongly couple to the microwave cavity photons [1–6]. In addition to such strong and ultra-strong magnon-microwave photon interaction, Zhang *et al.* demonstrated first in Ref. [7] that magnons can also couple with phonons through magnetostrictive interaction leading to magnomechanically induced transparency and absorption. Subsequently, the impact of magnon-induced dynamical back-action was also observed and analyzed [8,9]. The hybrid magnon-photon-phonon system, known as cavity magnomechanics, is a new platform for studying quantum effects at macroscopic scale, such as stationary entanglement [10–13], coherence [13], blockade [14], steering [15], and squeezing [16] for both magnons and phonons. In quantum information processing the cavity magnonics or magnomechanical system is suitable for realizing mature schemes like preparing Bell states (also Greenberger-Horne-Zeilinger and NOON states) [17–19], cooling mesoscopic objects to their ground states [20,21], and realizing quantum precision sensing [22]. The intersection of cavity magnomechanics with non-Markovian dynamics [23], accelerating adiabatic passages [24], and non-Hermitian quantum systems [25–27] are also hotspots in quantum optics.

Unlike the microwave-magnon beam splitter interaction, the magnetostrictive interaction is a radiation-pressure-like

interaction with nonlinearity [7,10]. Most of the work mentioned above, especially in continuous variables, tends to linearize this nonlinear interaction and restrict the quantum state to the Gaussian form [10,12,13,22,28–31]. Under semiclassical conditions, researchers have gradually focused on the bistability induced by magnetostrictive interactions, and a very recent experiment has confirmed some of those predictions [32]. These discussions focus on the fact that the nonlinearity can support a bistable asymptotic steady state but is not strong enough to excite the magnon to generate self-sustained oscillation. A quantum self-sustaining dynamics refers to a quantum evolution whose classical steady state forms a limit cycle in the phase space [33,34]. It associates with the mechanisms of diverse physics effects such as quantum phase transitions [35] and the spontaneous breaking of time-translation symmetry (quantum time crystal) [36,37], and provides a prerequisite for quantum phenomena such as quantum synchronization [38–40]. In the quantum regime, nonlinear effects induce the system to deviate from the Gaussian state and stabilize in a limit cycle state, which can be regarded as a mixture of Gaussians distributed over all the phases of the classical limit cycle orbit [41–44]. Previous work explored self-sustaining dynamics in optomechanics or van der Pol oscillators and has shown that some unique phenomena, such as multistability [41,44–46] and noise suppression [47], will emerge, which can never be observed in a linear system or treating nonlinear systems from a mean-field perspective. As an extension of optomechanics [48], cavity magnomechanics owns a new degree of freedom (DOF), i.e., the microwave-cavity DOF, leading to additional interactions and parameters (such as the coupling strength and detuning between magnon and microwave photons), which intuitively corresponds to a rich self-sustaining phase diagram. However,

*liwenlin@mail.neu.edu.cn

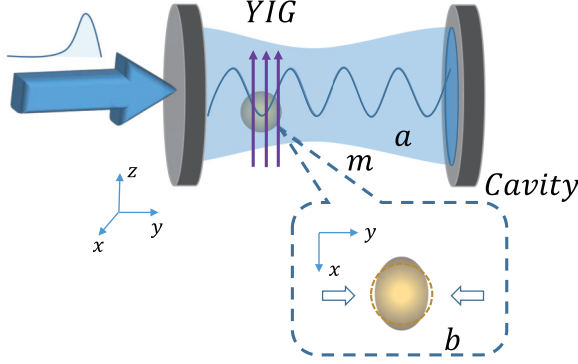


FIG. 1. Sketch of the considered cavity magnomechanics: A YIG sphere is placed inside a microwave cavity. The magnon mode m is coupled to the microwave mode a by the magnon-microwave photon interaction and to the mechanical mode b by the magnetostrictive interaction.

a systematic study of the self-sustaining dynamics in cavity magnomechanics has been difficult to achieve because the additional DOF complicates analytical analysis.

In this paper, we explore the nonlinear self-sustaining dynamics of standard cavity magnomechanics by generalizing the analysis of Marquardt *et al.* [45] and Rodrigues and Armour [47] via including the microwave-magnon beam splitter interaction. The microwave photon and magnon have high-order sidebands whose frequencies are integer multiples of the mechanical frequency, which can be solved by an iteration. We map out the attractors which suggest dynamics multistability for the limit cycles to the parameter space and verify numerically the analytic analysis by applying stochastic Langevin equations [41,44,49]. The results of the iterations allow us to predict the fluctuation distribution of the system, for example, phase spread, amplitude compression, and the mixture of different limit cycles. Moreover, the iteration results also allow us to predict the fluctuation distribution of the mechanical mode, such as phase diffusion, noise suppression, and the mixture of different limit cycles. Finally, we discuss the full quantum master equation of the self-sustaining systems to demonstrate the efficient range for observing quantum properties.

This paper is organized as follows: In Sec. II, we present the dynamics of the system, including iteratively solving attractors after deriving the slowly varying amplitude equation obtained after neglecting fast oscillating terms, and the rescaled stochastic Langevin equations. In Sec. III, we analyze the dynamical multistability in cavity magnomechanics. In Sec. IV, we study in detail the non-Gaussian dynamics of fluctuating distributions, such as phase diffusion, modulus noise suppression, and mixture of different limit cycle states. We finally show the quantum properties of the cavity magnomechanics in Sec. V by simulating the Lindblad master equation in a low excitation subspace. Conclusions and related discussions are given in the last section.

II. SYSTEM DYNAMICS

As shown in Fig. 1, we consider a standard cavity magnomechanics system consisting of a YIG placed inside a

microwave cavity and simultaneously in a uniform bias magnetic field [10]. The system Hamiltonian including the magnon-photon coupling and the magnetostrictive interaction reads

$$\begin{aligned} H/\hbar = & \omega_a \hat{a}^\dagger \hat{a} + \omega_m \hat{m}^\dagger \hat{m} + \omega_b \hat{b}^\dagger \hat{b} \\ & - g \hat{m}^\dagger \hat{m} (\hat{b}^\dagger + \hat{b}) + g_{ma} (\hat{a}^\dagger + \hat{a}) (\hat{m}^\dagger + \hat{m}) \\ & + i\Omega (\hat{m}^\dagger e^{-i\omega_a t} - \hat{m} e^{i\omega_a t}), \end{aligned} \quad (1)$$

where \hat{a} (\hat{a}^\dagger), \hat{m} (\hat{m}^\dagger), and \hat{b} (\hat{b}^\dagger) are the annihilation (creation) operators of the microwave cavity, the magnon mode, and the mechanical mode, and ω_a , ω_m , and ω_b are the corresponding resonance frequencies, respectively. g_{ma} denotes the magnon-microwave coupling rate, and g is the single-magnon magnomechanical coupling rate. Ω is the Rabi frequency satisfying $\Omega = \sqrt{5N} \gamma_g B_0 / 4$ [10,16], which denotes the coupling strength of the drive magnetic field with the magnon mode. Here γ_g is the gyromagnetic ratio. B_0 is the amplitude of the drive magnetic field satisfying $B_0 = R^{-1} (2P\mu_0/\pi c)^{1/2}$, where P is the pump power, R is the radius of YIG, and μ_0 and c are the permeability and the speed of light in vacuum. $N = \rho V$ is the total number of spins of the YIG, where ρ is the spin density in the YIG sphere, and V is the volume of the sphere.

The YIG and the cavity mode are coupled to their corresponding thermal reservoir at temperature T through fluctuation-dissipation processes yielding the following quantum Langevin equations in the frame rotating at the drive frequency ω_d [48,50,51]:

$$\begin{aligned} \dot{\hat{a}} = & (i\Delta_a - \kappa_a) \hat{a} - ig_{ma} \hat{m} + \sqrt{2\kappa_a} \hat{a}_{in}, \\ \dot{\hat{m}} = & (i\Delta_m - \kappa_m) \hat{m} - ig_{ma} \hat{a} + ig \hat{m} (\hat{b}^\dagger + \hat{b}) \\ & + \Omega + \sqrt{2\kappa_m} \hat{m}_{in}, \\ \dot{\hat{b}} = & (-i\omega_b - \gamma) \hat{b} + ig \hat{m}^\dagger \hat{m} + \sqrt{2\gamma} \hat{b}_{in}. \end{aligned} \quad (2)$$

In the above expressions, $\Delta_a = \omega_d - \omega_a$ ($\Delta_m = \omega_d - \omega_m$) is the drive-microwave (magnon) detuning, κ_a , κ_m , and γ are the dissipation rates of the cavity, magnon, and mechanical modes. \hat{a}_{in} , \hat{m}_{in} , and \hat{b}_{in} are the input noise operators corresponding to each mode. They are assumed to be white Gaussian fields obeying zero mean and standard correlation relations: $\langle \hat{o}_{in}^\dagger(t) \hat{o}_{in}(t') + \hat{o}_{in}(t') \hat{o}_{in}^\dagger(t) \rangle = (2\bar{n}_o + 1) \delta(t - t')$ for $o \in \{a, m, b\}$, where $\bar{n}_o = [\exp(\hbar\omega_o/k_b T) - 1]^{-1}$ is the mean thermal excitation number of the corresponding mode [50]. Here we have adopted the rotating-wave approximation (RWA) $g_{ma} (\hat{a}^\dagger + \hat{a}) (\hat{m}^\dagger + \hat{m}) \simeq g_{ma} (\hat{a}^\dagger \hat{m} + \hat{a} \hat{m}^\dagger)$ since the corresponding resonance frequencies $\omega_{a,m}$ are much larger than the coupling strength g_{ma} and the dissipation rates, which is easily satisfied in laboratory.

The nonlinear magnomechanical interaction may induce the mechanical mode to be in self-sustained oscillation, which will only have nonclassical properties when the excitation number is limited to several quanta and only corresponds to a small parameter domain. In most parameter domains, in contrast, the quantum state will remain non-negative in the Wigner representation during the whole dynamic process if the initial Wigner function is also non-negative [46,52]. Therefore the quantum Langevin equations in Eq. (2) can

be well approximated by a set of stochastic Langevin equations in which we replace operators \hat{a} , \hat{m} , and \hat{b} with c -number complex variables a , m , and b [41,44,46,49,53]. To get a universal conclusion and avoid our analysis being confined to some specific experimental parameters, we rescale the variables of our model as $\alpha = ga$, $\mathcal{M} = gm$, $\beta = gb$, and $E = \Omega g$ and the stochastic Langevin equations for the rescaled variables read

$$\begin{aligned}\dot{\alpha} &= (i\Delta_a - \kappa_a)\alpha - ig_{ma}\mathcal{M} + \sqrt{2\kappa_a}\alpha_{\text{in}}, \\ \dot{\mathcal{M}} &= [i(\Delta_m + (\beta^* + \beta)) - \kappa_m]\mathcal{M} - ig_{ma}\alpha + E + \sqrt{2\kappa_a}\mathcal{M}_{\text{in}}, \\ \dot{\beta} &= (-i\omega_b - \gamma)\beta + i|\mathcal{M}|^2 + \sqrt{2\gamma}\beta_{\text{in}},\end{aligned}\quad (4)$$

while the input operators are also replaced by rescaled classical complex random noises with modified correlation functions: $\langle \alpha_{\text{in}}^*(t)\alpha_{\text{in}}(t') \rangle = g^2(\bar{n}_o + 1/2)\delta(t-t')$ ($o \in \{a, m, b\}$) because the c numbers lose the commutation relation [41,49]. For each mode o , the corresponding quantum state can be solved by repeatedly calculating the stochastic Langevin equations N times (N should be large) and characterized by the expected value and the fluctuation, $\langle X \rangle = (1/N)\sum_i X^i$ and $\langle \delta^2 X \rangle = 1/(N-1)\sum_i [(X^i - \langle X \rangle)^2]$, where X can be any characteristic variable, and also characterized by the Wigner function, which is equivalent to the phase-space probability distribution in its non-negative case [51,52], that is,

$$W_o(Q, P) = \lim_{h \rightarrow 0} \frac{N_{Q,P}}{Nh^2}, \quad (4)$$

where $N_{Q,P}$ is the number of results satisfying $Q_o^i \in (Q - h/2, Q + h/2]$ and $P_o^i \in (P - h/2, P + h/2]$, with $Q_o^i = g(o^i + o^{i*})$ and $P_o^i = ig(o^{i*} - o^i)$ the two rescaled quadratures. Here the o^i is obtained by the i th stochastic trajectory in the simulation. The modulus distribution function and phase distribution function can also be defined in a similar logic as

$$P_\theta(\theta) = \lim_{h \rightarrow 0} \frac{N_\theta}{Nh}, \quad P_I(I) = \lim_{h \rightarrow 0} \frac{N_I}{Nh}. \quad (5)$$

In this paper, we mainly consider the self-sustaining solution of the mechanical mode which sets itself into a dynamics of the following form after an initial transient regime [44,45,47]:

$$\beta(t) = \beta_0 + Ae^{-i\omega_b t} = \beta_0 + |A|e^{-i(\omega_b t + \theta)}, \quad (6)$$

where β_0 and A are constants. The above treatment implies discarding the possible chaotic motion of the oscillator because it occurs only at extremely large driving powers and we will show in the follow-up discussions that this condition is not physically meaningful for the cavity magnomechanics we considered. In contrast, the nonlinear interaction will lead to the microwave mode and magnon mode showing complex dynamics accompanied by *distinguishable* higher-order sidebands, satisfying the following form:

$$\begin{aligned}\alpha(t) &:= \bar{\alpha} + \delta\alpha = \sum_n \alpha_n e^{in(\omega_b t + \theta)} + \delta\alpha, \\ \mathcal{M}(t) &:= \bar{\mathcal{M}} + \delta\mathcal{M} = \sum_n \mathcal{M}_n e^{in(\omega_b t + \theta)} + \delta\mathcal{M},\end{aligned}\quad (7)$$

where $\bar{\alpha}(\bar{\mathcal{M}})$ is the expected value solution obtained when the stochastic force term α_{in} (\mathcal{M}_{in}) is dropped and $\delta\alpha$ ($\delta\mathcal{M}$) describes the perturbation of the corresponding input noise. We first formally solve the stochastic Langevin equation (3) by substituting Eqs. (6) and (7), and by neglecting the transient term related to the initial value we have the expected value parts:

$$\bar{\alpha}(t) = \int_0^t dt' e^{\mathcal{L}_a(t-t')} \left[-ig_{ma} \sum_n \mathcal{M}_n e^{in(\omega_b t' + \theta)} \right] \quad (8)$$

and

$$\begin{aligned}\bar{\mathcal{M}}(t) &= \int_0^t dt' \left\{ e^{\mathcal{L}_m(t-t')} \left[\sum_n \alpha'_n e^{in(\omega_b t' + \theta)} \right] \right. \\ &\quad \left. \times \exp \left[2i \int_{t'}^t dt'' |A| \cos(\omega_b t'' + \theta) \right] \right\},\end{aligned}\quad (9)$$

where we define $\mathcal{L}_{a,m} = i[\Delta_{a,m} + (\beta_0 + \beta_0^*)] - \kappa_{a,m}$, $\alpha'_n = -ig_{ma}\alpha_n + E\delta(n)$ for convenience. For a common oscillator with a high Q factor [32], the order of the characteristic time corresponding to the dynamics of amplitude is γ^{-1} , which is much slower than the fast oscillations at ω_b . One thus can adopt treating the amplitude as a constant in the integral over t'' in Eq. (9), i.e., adopting the Markovian approximation. Performing explicitly this integral, one gets

$$\bar{\mathcal{M}}(t) = e^{i\psi(t)} \int_0^t dt' e^{\mathcal{L}_m(t-t')} \left[\sum_n \alpha'_n e^{in(\omega_b t' + \theta)} \right] e^{-i\psi(t')}, \quad (10)$$

where $\psi(t) = \xi \sin(\omega_b t + \theta)$, with $\xi = 2|A|/\omega_b$. The phase factor $e^{-i\xi \sin \phi}$ can be expanded by the Jacobi-Anger expansion $e^{-i\xi \sin \phi} = \sum_n J_n(-\xi) e^{in\phi}$ where J_n is the n th Bessel function of the first kind. One obtains the following solutions for the optical and magnon modes, after the integration:

$$\bar{\alpha}(t) = \sum_{n=-\infty}^{\infty} \frac{-ig_{ma}\mathcal{M}_n e^{in(\omega_b t + \theta)}}{in\omega_b - \mathcal{L}_a} \quad (11)$$

and

$$\bar{\mathcal{M}}(t) = \sum_{N,M,n=-\infty}^{\infty} \frac{\alpha'_N J_M(-\xi) J_{N+M-n}(-\xi) e^{in(\omega_b t + \theta)}}{i(N+M)\omega_b - \mathcal{L}_m}. \quad (12)$$

The coefficients in the above equations can be solved by the iterative method under the condition that g_{ma} is relatively weak ($g_{ma}/\omega_b < 0.4$ in the following calculations), and we finally determine a series of iterative equations [54]:

$$\begin{aligned}\alpha_n^j &= -ig_{ma}\alpha_n^j + E\delta(n), \\ \mathcal{M}_n^j &= \sum_{N,M=-\infty}^{\infty} \frac{\alpha_N^j J_M(-\xi) J_{N+M-n}(-\xi)}{i(N+M)\omega_b - \mathcal{L}_m}, \\ \alpha_n^{j+1} &= \frac{-ig_{ma}\mathcal{M}_n^j}{in\omega_b - \mathcal{L}_a}.\end{aligned}\quad (13)$$

The trial solution of the above equations is selected as $\alpha_n^0 = 0$ which leads to $\alpha_n^0 = E\delta(n)$ and $\mathcal{M}_n = E \sum_m J_m(-\xi) J_{m-n}/(im\omega_b - \mathcal{L}_m)$. Physically, these trial solutions correspond to the dynamics when the optical

mode and the magnon mode are decoupled, so that they are consistent with the conclusions of the previous study on the nonlinearity of single optomechanics [45]. \mathcal{M}_n and α_n can be finally determined after the errors have converged to an acceptable range through several iterations, i.e., $|\mathcal{M}_n^{j+1} - \mathcal{M}_n^j| < \eta$ and $|\alpha_n^{j+1} - \alpha_n^j| < \eta$, where $\eta < 10^{-20}$ is the criterion we set to constrain the accuracy of the later results, and for most points on the phase diagram 10–20 iterations are sufficient to achieve this accuracy.

Repeating the above substitution and removing the part of the expectation values given by Eqs. (8) and (9), the fluctuation terms can be obtained as

$$\delta\alpha(t) = \sqrt{2\kappa_a} \int_0^t dt' e^{\mathcal{L}_a(t-t')} \left[-i \frac{g_{ma}}{\sqrt{2\kappa_a}} \delta\mathcal{M}(t') + \alpha_{\text{in}}(t') \right] \quad (14)$$

and

$$\delta\mathcal{M}(t) = \sqrt{2\kappa_m} e^{i\psi(t)} \int_0^t dt' e^{\mathcal{L}_m(t-t')} \left[-i \frac{g_{ma}}{\sqrt{2\kappa_m}} \delta\alpha(t') e^{-i\psi(t')} + \mathcal{M}_{\text{in}}(t') \right]. \quad (15)$$

Note that $\mathcal{M}_{\text{in}}(t) e^{-i\psi(t)}$ possesses the same correlation functions of $\mathcal{M}_{\text{in}}(t)$ and therefore the factor related to the magnon mode can be practically neglected in the integral for convenience. Thus, the magnon term can be written as $|\mathcal{M}|^2 \simeq |\tilde{\mathcal{M}}|^2 + \tilde{\mathcal{M}}\delta\mathcal{M}^* + \tilde{\mathcal{M}}^*\delta\mathcal{M}$, where

$$|\tilde{\mathcal{M}}|^2 = \sum_{N, N', M, n=-\infty}^{\infty} \frac{\alpha'_N \alpha'_{N'} J_m(-\xi) J_{N+M-n}(-\xi) e^{in(\omega_b t + \theta)}}{[i(N+M)\omega_b - \mathcal{L}_m][i(N+M-n)\omega_b - \mathcal{L}_m^*]}. \quad (16)$$

Substituting the magnon term $|\mathcal{M}|^2$ into the Langevin equations related to β , we have

$$\dot{\beta}_0 = (-i\omega_b - \gamma)\beta_0 + i \sum_{N, N', M=-\infty}^{\infty} \frac{\alpha'_N \alpha'_{N'} J_m(-\xi) J_{N+M}(-\xi)}{[i(N+M)\omega_b - \mathcal{L}_m][i(N+M)\omega_b - \mathcal{L}_m^*]} \quad (17)$$

and

$$\dot{A} = \left(-\gamma - \frac{i}{|A|} \sum_{N, N', M=-\infty}^{\infty} \frac{\alpha'_N \alpha'_{N'} J_m(-\xi) J_{N+M+1}(-\xi)}{[i(N+M)\omega_b - \mathcal{L}_m][i(N+M+1)\omega_b - \mathcal{L}_m^*]} \right) A + \sqrt{2\gamma} \beta_{\text{in}}, \quad (18)$$

and the other terms with different frequencies are neglected by RWA. Here we define a dimensionless auxiliary function:

$$\mathcal{F}(|A|, \Delta_{m,a}, g_{ma}, \gamma) = -\frac{i}{\gamma|A|} \sum_{N, N', M=-\infty}^{\infty} \frac{\alpha'_N \alpha'_{N'} J_m(-\xi) J_{N+M+1}(-\xi)}{[i(N+M)\omega_b - \mathcal{L}_m][i(N+M+1)\omega_b - \mathcal{L}_m^*]}, \quad (19)$$

which leads Eq. (18) to be in the following compact form:

$$\dot{A} = [-\gamma(1 - \mathcal{F})]A + \xi, \quad (20)$$

where $\xi = \sqrt{2\gamma} \beta_{\text{in}} + i(\tilde{\mathcal{M}}\delta\mathcal{M}^* + \tilde{\mathcal{M}}^*\delta\mathcal{M})$ is a modified noise composed of white Gaussian noise (the first term) and color noise (the last two terms). Calculating the correlation function of color noise involves more tedious iterative solutions, but its magnitude can be roughly estimated from the results of the zeroth-order iteration, that is, following the related research on optomechanics [47]. In the case of $(\kappa_m/\Delta_m)^2 \ll 1$, the effect of the color noise scales with $g^2 \Omega^2 J_0(-\xi)^2 \bar{n}_m / \kappa_m \Delta_m^2 = E^2 J_0(-\xi)^2 \bar{n}_m / \kappa_m \Delta_m^2$ while the effect of the white noise is $\gamma \bar{n}_b$. Thus, by assuming that the reservoir surrounding each mode corresponds to the same temperature, the effects of thermal and microwave-magnon noises are comparable only when the cooperativity $C = E^2 J_0(-\xi)^2 / \kappa_m \gamma \Delta_m^2$ is comparable to $\bar{n}_b / \bar{n}_m = \omega_m / \omega_b$. With the parameters we have chosen, this condition is always far from being satisfied, even if we consider a high Q -factor mechanical mode ($Q = \omega_b / \gamma = 10^6$).

The \mathcal{F} function contains all the information about the self-sustaining dynamics of the cavity magnomechanics system except for the input noise terms, and we will explain in detail

how to analyze the corresponding nonlinear properties according to the \mathcal{F} function in a later section.

III. DYNAMICAL MULTISTABILITY IN CAVITY MAGNOMECHANICS

We first analyze the dynamical multistability of the considered cavity magnomechanics by establishing stability conditions and deriving corresponding attractors, which can give all the information of the nonlinear properties compared with a numerical simulation. By rewriting Eq. (21) in terms of the modulus and phase of the complex amplitudes $A = |A|e^{i\phi} := Ie^{i\phi}$ and adopting the mean-field approximation, the corresponding noiseless equation of the modulus reads

$$\dot{I} = [-\gamma(1 - \text{Re}(\mathcal{F}))]I, \quad (21)$$

and this equation describes the self-sustaining dynamics of the cavity magnomechanics. For the occurrence of stable dynamics, the modulus of the limit cycle I_s should satisfy the following two conditions:

$$1 - \text{Re}[\mathcal{F}(I_s)] = 0 \quad (22)$$

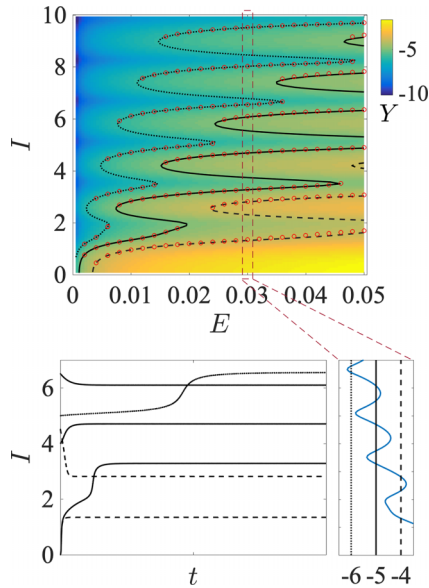


FIG. 2. Multistability phase diagram and attractors in terms of $Y = \log_{10}[(\gamma/\omega_b)\text{Re}(\mathcal{F})]$ in the modulus-rescale driving plane. The dash, solid, and dot lines denote the contour lines -4 , -5 , and -6 and the corresponding red cycles are the simulation results with $\gamma/\omega_b = 10^{-4}$, 10^{-5} , and 10^{-6} , respectively. The other dimensionless parameters are $\Delta_a = -1$, $\Delta_m = 1$, $g_{ma} = 0.2$, and $\kappa_a = \kappa_m = 0.1$ with $\omega_b = 1$ as the unit. The bottom panel shows the correspondence of the attractor to the steady states. The blue line in the right inset is a cross-sectional view of the phase diagram with $E = 0.03$ and on the left are the long-time dynamics with different initial states under the corresponding parameters.

and

$$\frac{d}{dI}[\text{Re}(\mathcal{F})]|_{I=I_s} < 0. \quad (23)$$

The first condition describes the dissipation-gain balance mechanism of the mechanical mode, while the second condition ensures that the error will converge to these equilibrium points, i.e., the equilibrium point should correspond to a stable equilibrium, but not unstable equilibrium or intermediate equilibrium. Since the function \mathcal{F} is composed of Bessel functions that have periodicity, Eq. (22) may have multiple solutions, which means the occurrence of multistability.

In Fig. 2, we show the multistability phase diagram in terms of $Y = \log_{10}[(\gamma/\omega_b)\text{Re}(\mathcal{F})]$ in the modulus-rescale driving plane. Each contour line with a value of s means that Eq. (22) is satisfied under the parameter condition of $\gamma/\omega_b = 10^s$, which is a necessary condition for forming a steady state as we mentioned above. In addition, the \mathcal{F} function has a peak-trough structure so that the sign of the corresponding derivative changes alternately, while the greater-than-zero part denotes metastable states. Excluding the metastable states, the remaining contour lines still have multiple intersections with those lines paralleling to the longitudinal axis representing constant values of E , which indicates the occurrence of multistability. The red points in Fig. 2 denote the numerical results corresponding to different initial values. They are obtained by simulating (3) without noise terms until their evolution converges. They show a perfect fit

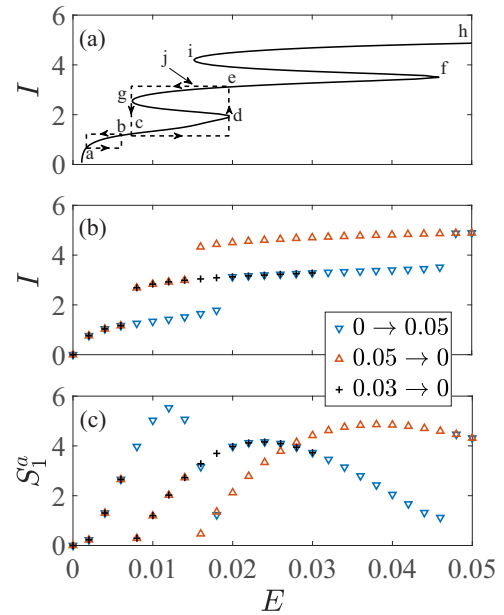


FIG. 3. (a) The contour line corresponding to $\gamma/\omega_b = 10^{-5}$ in the phase diagram 2. (b), (c) Multistable mechanical modulus and spectra of microwave modes vs the drive power. In (c), $S_1^a = 10^5 \times \max[S^a(0.96\omega_b - 1.06\omega_b)]$, that is, the amplitude of the first main peak. The arrows indicate the starting point and direction of sweeping the parameter. The variance of the related noise we set in this simulation is $\bar{n}'_b = 10^{-9}$ and the other parameters are the same as in Fig. 2.

with the upper half of each elliptical contour and never touch the lower half of the orbit as expected. Figure 2 also shows the number of steady limit cycles and their corresponding radii increase with the increase of driving and oscillator quality factors, consistent with our physical intuition.

A dynamic detection process is usually accomplished by continuously and weakly measuring the evolution in a specific experiment instead of repeating the same experiment many times and observing the system at different moments. The whole process will correspond to a single stochastic trajectory and the room-temperature environment is not sufficient to support its transition to other steady states based on the fluctuation effect alone. In this case, the multistability can be manifested by observing the hysteresis loop after scanning the parameters along different paths, i.e., slowly increasing the pump intensity from zero to a fixed value E_c and then gradually decreasing it to zero. Such hysteresis loop can also be predicted from the phase diagram. As an example, we discuss the case of $\gamma/\omega_b = 10^{-5}$, which corresponds to the solid contour line in Fig. 2 and we also plot it in Fig. 3(a). A complete parameter scan in the monostable interval (e.g., the dashed path on the left) gives exactly the same trend in amplitude in both directions ($a \rightarrow b \rightarrow a$), i.e., no hysteresis effect occurs. It is worth noting that the appearance of bistability does not mean that hysteresis effects must be observed, since the lower-energy steady state “c” prevents the system from being excited to another steady state “g.” Such a higher-energy steady state occurs until the pump is sufficiently strong to support the jump ($d \rightarrow e$) when the lower steady state disappears. Accordingly, decreasing the pump at this point will not bring

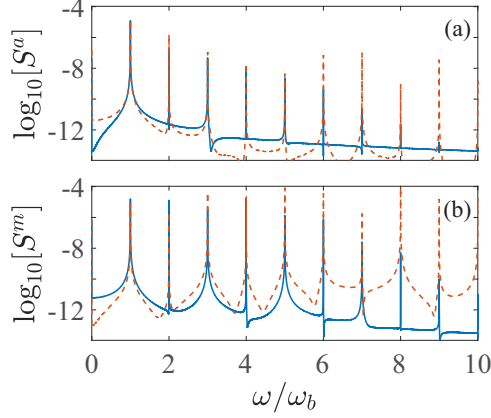


FIG. 4. Spectrum analysis of microwave mode (a) and magnon mode (b) corresponds to accidental degenerate points at $E = 0.018$. The blue solid line corresponds to the blue mark and the red dotted line corresponds to the red mark in Fig. 3. The other parameters are the same as in Fig. 2.

the system back to steady state “d” immediately, but only after point “g,” when the higher steady state disappears. We thus obtain the path of the amplitude variation as $a \rightarrow d \rightarrow e \rightarrow f \rightarrow g \rightarrow c \rightarrow a$, where the range of hysteresis effects is $E \in [c, d]$, corresponding to the right dashed path in Fig. 3(a). Under similar logic, the corresponding path for the tristable state is $a \rightarrow d \rightarrow e \rightarrow f \rightarrow h \rightarrow i \rightarrow j \rightarrow g \rightarrow c \rightarrow a$.

In Fig. 3(b) we sweep the pump intensity E bidirectionally in the range $[0, 0.03]$ and $[0, 0.05]$, respectively, and plot the simulation result of the steady-state modulus. It can be seen that the scattering point as well as the hysteresis effects have a consistent correspondence with the paths we predicted in Fig. 3(a), implying that there are at least two steady states. In addition, two hysteresis paths and the triple steady state (three separate points at $E = 0.018$) can also be observed. Taking $g = 2\pi \times 1(0.1)$ Hz gives $g/\omega_b = 10^{-7}(10^{-8})$ for $\omega_b = 2\pi \times 10$ MHz, so the original parameter corresponding to the critical drive (point “d”) for observing bistability will be $\Omega/\omega_b \approx 2 \times 10^5(10^6)$, and $5 \times 10^5(10^6)$ for observing tristability. The requirements for observing tristability can be further reduced to $E = 0.15$, leading to $\Omega/\omega_b \approx 1.5 \times 10^5(10^6)$ under the condition of $\gamma/\omega_b = 10^{-6}$. This driving intensity is achievable under existing experimental conditions.

The dynamics of the mechanical mode can be probed by the homodyne detection and spectral analysis of the output field of the microwave mode, which is proportional to the microwave mode itself while neglecting the vacuum noise, that is,

$$S_{\text{out}}^a(\omega) = \left| \frac{1}{\sqrt{2\pi}} \int dt \{ \text{Im}[\sqrt{\kappa_a} \alpha(t) + \alpha_{\text{in}}] \} \right|^2, \\ \propto S^a(\omega) = \left| \frac{1}{\sqrt{2\pi}} \int dt \{ \text{Im}[\alpha(t)] \} \right|^2. \quad (24)$$

Equations (11) and (12) reveal that both the magnon mode and the microwave mode are excited into their higher-order sidebands [55,56], which will be shown later in Fig. 4. Here we consider the height of the first-order sideband peak during the parameter scanning to characterize the multistability and

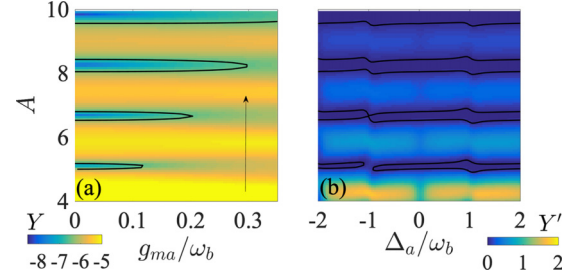


FIG. 5. Multistability phase diagram and attractors in terms of $Y = \log_{10}[(\gamma/\omega_b)\text{Re}(\mathcal{F})]$ in the modulus-magnon-microwave coupling plane (a) and in terms of $Y' = (\gamma/\omega_b)\text{Re}(\mathcal{F})$ in the modulus-detuning plane (b). The absence of logarithmic coordinates in (b) is due to the presence of negative values (the left end of the colorbar is -0.05) and we magnified the data 10^6 times for convenience. The black solid lines correspond to $\gamma/\omega_b = 10^{-6.5}$. Here we set $E = 0.02$ and the other parameters are the same as in Fig. 2.

show the related hysteresis curves in Fig. 3(c). It shows a perfect correspondence between the magnon hysteresis and the mechanical hysteresis. The only thing worth noting is that the nonlinear mapping causes $S_1^a \propto A$ no longer to hold and $S_1^a(A) = S_1^a(A')$ is not sufficient to infer $A = A'$, i.e., the microwave spectra of two different moduli have the same value at the first-order sideband, such as the overlapping blue and red markers at $E = 0.018$ in Fig. 3(c). We call such a case “accidental degeneracy,” and they can be distinguished by comparing the corresponding high-order sidebands. In Fig. 4(a), we plot the spectrum of this accidental degenerate point. It shows intuitively that although they have a similar peak at the first-order sideband the rest of the high-order sidebands are entirely different, implying that they hide two steady limit cycles. We also demonstrate that the magnon mode has diverse higher-order sideband peaks, as expected and shown in Fig. 4(b). Moreover, Fig. 4 also verifies an assumption in our derivation, namely, that the sidebands of the system are distinguishable so that their respective dynamics are sufficiently independent [57].

Compared with the standard cavity optomechanical system, the magnon DOF allows us to control the self-sustaining dynamics of the mechanical mode under the guidance of the \mathcal{F} function and attractors. In Fig. 5(a), we show the quantitative dependence of the \mathcal{F} function on magnon-microwave coupling g_{ma} and mark a set of contours corresponding to $\gamma/\omega_b = 10^{-6.5}$. It can be seen that the increased g_{ma} gradually inhibits the emergence of low-energy limit cycles, that is, if we choose a thermal state as the initial mechanical state, which is typically the case, we can directly excite it to a larger limit cycle by adjusting g_{ma} without being “intercepted” by those low-energy steady states. The mechanism can lead to a strong phonon laser with high energy in cavity magnomechanics. In Fig. 5(b), we discuss the influence of the frequency detuning Δ_a on self-sustaining dynamics with a fixed pump intensity and g_{ma} . In contrast, the influence of Δ_a on the \mathcal{F} function is relatively insignificant, and it only affects the steady state at an integer multiple of the sideband (for example, the contour is broken at $\Delta_a = -1$, meaning that a steady state is forbidden under this parameter). It can be considered that the self-sustaining system is robust to the detuning.

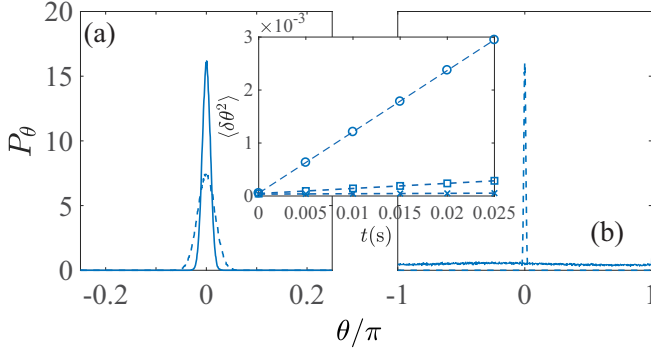


FIG. 6. (a) Phase probability distribution of the mechanical mode at $t = 0$ s (solid) and 0.025 s (dashed) in the case of $\gamma/\omega_b = 10^{-4}$. (b) The phase probability distribution of the mechanical mode at $t = 0.005$ s corresponds to the initial state satisfying $\langle \beta \rangle = 0$ (solid) and $\langle \beta \rangle = 0.96$ (dash). The data corresponding to the solid line in (b) is tripled for ease of presentation. The inset plot shows the evolution of the phase fluctuations, where the circle, square, and cross markers denote the cases $\gamma/\omega_b = 10^{-4}$ and $E = 0.01$, $\gamma/\omega_b = 10^{-5}$ and $E = 0.004$, and $\gamma/\omega_b = 10^{-6}$ and $E = 0.002$, respectively, and the dashed lines are the corresponding fit results. The results are obtained by 100 000 realizations of the stochastic Eqs. (3). In this simulation we set $\bar{n}'_b = 10^{-4}$ and the other parameters are the same as in Fig. 2.

IV. PHASE DIFFUSION, MODULUS NOISE SUPPRESSION, AND MIXTURE OF MULTIPLE LIMIT CYCLE STATES

The fluctuation-dissipation process and the corresponding distribution of the self-sustained dynamics are relevant to a variety of studies such as phonon lasers, precision signal detection, quantum synchronization, etc. In this section, we analyze it analytically through the properties of the \mathcal{F} function, thus avoiding the incompleteness of the mean-field approach and the time consumed by numerical simulations. Let us reconsider Eq. (21) but with the noise term, and the corresponding modulus and phase equations are

$$\dot{I} = [-\gamma(1 - \text{Re}(\mathcal{F}))I + \sqrt{2\gamma}I_{\text{in}}] \quad (25)$$

and

$$\dot{\phi} = -\frac{\text{Im}(\mathcal{F})\gamma}{I\omega_b} + \frac{\sqrt{2\gamma}}{I}\phi_{\text{in}}. \quad (26)$$

Equation (26) describes stochastic dynamics with only fluctuating processes but no corresponding dissipation processes, meaning that the growth of phase variance is never suppressed. Physically, infinite phase variance means that the probability distribution of the system will uniformly disperse on the classical limit cycle in the phase space. Complete dephasing occurs at this time since the oscillator completely loses its phase. Under the condition that a stable limit ring can be formed, the order of the phase free diffusion rate is

$$\eta_P \sim \frac{\gamma n_{\text{th}}}{I_s^2}, \quad (27)$$

and the time for complete phase diffusion is approximately $t \approx \pi^2/\eta_P = \pi^2 I_s^2/\gamma n_{\text{th}}$. In Fig. 6(a), we simulate the phase probability distribution of the oscillator in the monostable parameter region with the initial state selected as a

translational thermal state centered at the noiseless limit cycle orbit. The probability distribution becomes flatter, meaning the oscillator deviates from the Gaussian state. In the inset, we plotted the evolution of phase fluctuations $\langle \delta\theta^2 \rangle$ over time. We find that they can be perfectly linearly fitted with the slopes satisfying $k/\eta_P = 1.048$ for $\gamma/\omega_m = 10^{-4}$, $k/\eta_P = 1.029$ for $\gamma/\omega_m = 10^{-5}$, and $k/\eta_P = 1.014$ for $\gamma/\omega_m = 10^{-6}$, respectively, meaning that the numerical results are consistent with the derived diffusion rate. It can also be inferred that the probability distribution of the mechanical mode will completely disperse on the limit cycle after $\gamma t \approx 10^5$.

The transient dynamics in the initial stage will be more complicated if the initial state is far away from the limit cycle. In particular, the initial state in experiments usually corresponds to a thermal state while the mechanical mode is pumped to the limit cycle by the gain effect accompanied by an inflation of the fluctuation, thereby accelerating the phase diffusion degree of the oscillator as shown in Fig. 6(b). Therefore, for the nonlinear self-sustained magnomechanics, the Gaussian mean-field approximation and the linearization analysis of fluctuations are no longer reliable, although they may hold in a short regime [49,53,58], that is, the non-Gaussianity caused by the dephasing process is not obvious, which depends on the nonlinear parameters as well as the bath temperature.

The dephasing phenomenon can also be explained from another perspective: We have divided the Langevin equation into two equations for variables β_0 and A and each of which corresponds to an effective Hamiltonian consisting of $H_{\text{eff}}(\beta_0)$ and $H_{\text{eff}}(A)$, where $H_{\text{eff}}(A)$ satisfies the U(1) symmetry although $H_{\text{eff}}(\beta_0)$ is asymmetric, resulting in the Hamiltonian (1) having no such symmetry. Under the occurring limit cycle, β_0 only describes the translation distance of its center in the phase space and satisfies $A \gg \beta_0$. $H_{\text{eff}}(A)$ occupies a dominant position, and the total Hamiltonian we considered degenerates into U(1) symmetrical so that the steady state corresponding to a Markovian dynamics must be a phase independent state in phase space. The modulus, as another observable information of the magnomechanics, can be used to determine certain parameters of the system, such as the intensity of the nonlinear interaction [59], or the amplification of weak signals in some designed measurement schemes represented by the ‘‘latching’’ measurement [45,60]. Thus, compressing the modulus fluctuation could improve the signal-to-noise ratio of these schemes or avoid false positive signals, thereby improving the measurement accuracy. Moreover, the self-sustained dynamics of the mechanical mode can also be used to achieve a phonon laser, whose coherence requires the case of low-energy fluctuations [61]. The fluctuation of the modulus is calculated by the standard linearization method, i.e., consider I as a sum of its expectation value and a small fluctuation (δI) near the expectation value. By removing terms related to the expectations from Eq. (25), we have

$$\delta \dot{I} = \left[-\gamma \left(1 - \text{Re}(\mathcal{F}) - I \frac{d\text{Re}(\mathcal{F})}{dI} \right) \right] \delta I + \sqrt{2\gamma} I_{\text{in}}. \quad (28)$$

When a stable limit cycle occurs, the term $1 - \text{Re}(\mathcal{F})$ will vanish from the right-hand side of the above equation, and we

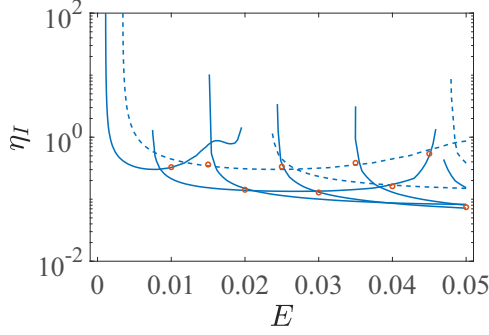


FIG. 7. Amplitude noise compression ratios as a function of rescale pump intensity E corresponding to $\gamma/\omega_b = 10^{-4}$ (dash) and $\gamma/\omega_b = 10^{-5}$ (solid), respectively. The red cycles are corresponding simulation results obtained by 20000 realizations of the stochastic equations. The other parameters are the same as in Fig. 2.

can therefore define the compression ratio as follows:

$$\eta_I = \frac{I_n}{I_{n_{th}}} = \frac{2}{4 - \pi} \left(-I_S \frac{d\text{Re}(\mathcal{F})}{dI} \Big|_{I=I_S} \right)^{-1}, \quad (29)$$

where $I_n = \langle \delta I^2 \rangle$ is the amplitude fluctuation when the oscillator is driven to the limit cycle, and $I_{n_{th}}$ is the amplitude fluctuation when the oscillator is not driven, i.e., in a thermal state. The correction factor $(4 - \pi)/2$ comes from the fact that the modulus of a thermal state satisfies the Rayleigh distribution. In Fig. 7, we show a series of analytically derived compression ratios with varied rescaled driving intensity E . The solid and dashed lines distinguish the cases of $\gamma/\omega_b = 10^{-4}$ or 10^{-5} , and the cycles denote numerical results as supporting evidence. It demonstrates that the modulus is not always compressed. However, a heating effect occurs in a small range of E , corresponding to a weak driving regime. With the parameters considered, the optimum compression ratio can be of the order of 10^{-2} . In addition, there are multiple different compression ratios under the same parameters due to the multistability. In practical application scenarios, one can select the optimal one by designing the parameter scan path mentioned above.

For a system with multistability, the input noise and initial fluctuation may induce the stochastic trajectory to jump to different stable states, resulting in a distribution function that is no longer a single cycle but a mixture of multiple limit cycle states. The inset in Fig. 8 shows that the probability distribution function owns a double-ring structure in the phase space. A more quantitative description is shown in Fig. 8 by plotting its corresponding modulus distribution function, which owns a bimodal structure. Each peak is relatively independent, satisfying our analysis of the unimodal distribution above, and can be well described by Eq. (28). The distribution will be more inclined to the steady state with higher energy by increasing the noise or nonlinear coupling g while holding $E = g\Omega$ constant. It is worth emphasizing that, as a nonlinear effect, the critical rescale noise of the double-ring structure under the selected parameters is of the order of $\bar{n} = 10^{-1}$ in which case the corresponding g should be a few kilohertz at room temperature. It is several orders of magnitude larger than the bare magnomechanical coupling strength achieved in

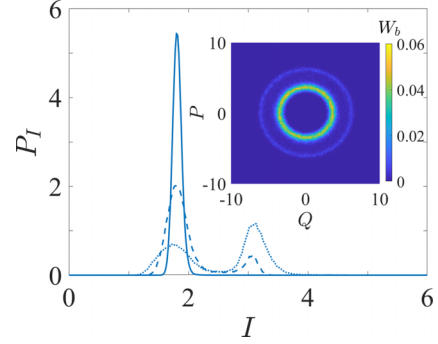


FIG. 8. Modulus distribution function of the mechanical mode at $\gamma t = 5$ corresponding to $\bar{n}_b' = 0.04$ (solid), 0.25 (dash), and 1 (dot), respectively. The subfigure denotes the Wigner function (phase-space probability distribution) of the mechanical mode corresponding to the dash line case. The results are obtained by 100 000 realizations of the stochastic equations and the other parameters are the same as in Fig. 2.

the experiments [7,32]. Heating the thermal reservoir around the mechanical mode, which makes the Brownian effect more significant, can reduce the critical nonlinear coupling [62]. On the other hand, the disturbance of the experimental equipment itself will cause parameters such as g_{ma} , g , and Ω to have fluctuations, which can be seen as additional noise terms in the dynamical equations, e.g., replace g in Eq. (2) with $g + \mathcal{N}$, where \mathcal{N} is a white Gaussian noise. These disturbing noises may also induce the double-ring distribution function with lower nonlinearity.

V. FULL QUANTUM SELF-SUSTAINING DYNAMICS

In the semiclassical analysis, the driving and nonlinear coupling strength degenerate into a joint parameter $E = \Omega g$, rather than affecting the dynamics of the rescaled variables independently. Considering the mapping between the actual dynamics of the oscillator and the rescaled variables $b = \beta/g$ and the fact that the modulus $A = |\beta|$ on a scale of less than 10^1 , the excitation of the oscillator will reduce to several quanta in the strong nonlinearity regime, which refers to the coupling coefficient g in the same magnitude as ω_m . The quantum effect will become significant in this interval, and the system will deviate from semiclassical dynamics. The full quantum dynamics of the cavity magnomechanics is described by the following master equation [63]:

$$\begin{aligned} \dot{\rho} = & i[\rho, H] + \kappa_a \mathcal{D}[\hat{a}] \rho + \kappa_m \mathcal{D}[\hat{m}] \rho \\ & + \gamma(n_{th} + 1) \mathcal{D}[\hat{b}] \rho + \gamma n_{th} \mathcal{D}[\hat{b}^\dagger] \rho, \end{aligned} \quad (30)$$

where $\mathcal{D}[o]\rho = 2\delta\rho\delta^\dagger - \delta^\dagger\delta\rho - \rho\delta^\dagger\delta$ is the standard form of the Lindblad superoperator. The density matrix ρ corresponding to a steady state can be described by taking the left-hand side of the above expression to zero, and we solve it by representing the whole equation in the Hilbert space with Fock basis and truncate the high-dimensional space because the number of excitations is not high. The quantum state of the mechanical mode is fully characterized by the Wigner

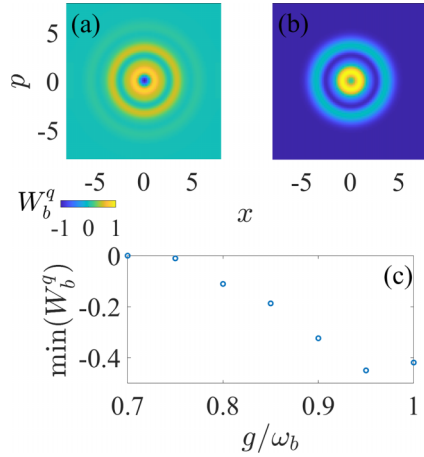


FIG. 9. (a), (b) Full quantum Wigner function W_b^q corresponding to $g/\omega_b = 1$ and 0.7 respectively. (c) Minimum value of the Wigner function as a function of the magnomechanical coupling g . The simulation results were obtained by solving the steady-state solutions of Eq. (31) in a truncated Hilbert space whose dimension is from $(3 \times 3)_a \otimes (3 \times 3)_m \otimes (35 \times 35)_b$ to $(3 \times 3)_a \otimes (3 \times 3)_m \otimes (60 \times 60)_b$ depending on the convergence of the results [64]. Here we set $\gamma/\omega_b = 10^{-5}$, $E = 0.02$, and $\bar{n}_{\text{th}} = 0$. The other parameters are the same as in Fig. 2.

function, which is defined as follows [51]:

$$W_o^q(x, p) = \frac{1}{\pi} \int_{-\infty}^{\infty} dy \langle x - y | \rho_o | x + y \rangle e^{2ipy}, \quad (31)$$

where ρ_o is the reduced density operator of the mode o .

In Fig. 9(a), we show the Wigner function corresponding to full quantum analysis and find that it has significant nonclassical properties, manifested in the appearance of negative values of the Wigner function, under conditions where g is comparable to ω_b in magnitude. In Fig. 9(b), we reduce the magnomechanical coupling to $g/\omega_b = 0.7$ while increasing the drive Ω keeping E constant and the whole system corresponds to a smaller “quantum parameter” [41,65]. It can be seen that the the Wigner function is non-negative in this case, meaning that the mechanical mode degenerates into a “classical” state. A more detailed demonstration is plotted in Fig. 9(c) where we plot the minimum value of the Wigner function as a function of the magnomechanical coupling g . Under the parameters we consider, the critical condition for observing the quantum nature of the self-sustained dynamics is $g/\omega_b = 1$, a very stringent requirement for the existing experimental techniques. It, therefore, proves that the semiclassical stochastic Langevin equations adopted in the above sections are accurate enough for general parametric conditions.

VI. DISCUSSION AND CONCLUSION

Here we summarize the parameter conditions corresponding to all the nonlinear phenomena predicted in the above section. In addition to the rescaled parameters, we also consider a realistic scenario corresponding to $\omega_a = \omega_m = 2\pi \times 10$ GHz, $g_{ma} = 2\pi \times 2$ MHz, $\kappa_a = \kappa_m = 2\pi \times 1$ MHz, and $\gamma_g = 2\pi \times 28$ GHz/T [7,32]. As examples, we consider

TABLE I. Critical parameters in realistic scenarios.

	Q	E	B_0 (μT)		Power (mW)	
			YIG 1	YIG 2	YIG 1	YIG 2
Bistability	10^5	0.019	13.1	25.8	1.0	0.63
	10^6	0.006	4.1	8.2	0.10	0.062
Tristability	10^5	0.046	31.6	62.5	5.9	3.7
	10^6	0.014	9.6	19.0	0.54	0.34
ANC	10^4	0.0055	3.8	7.5	0.084	0.052
	10^5	0.0017	1.2	2.3	0.0080	0.005

two YIG spheres, where YIG 1 is of $R = 125 \mu\text{m}$ and $g = 2\pi \times 50$ MHz and YIG 2 is of $R = 50 \mu\text{m}$ and $g = 2\pi \times 100$ MHz [66]. Under the two sets of parameters, we list in Table I the minimum magnetic fields and the corresponding powers for which bistable, tristable, and amplitude noise compression (ANC) can be observed. A much higher power $P > 10$ mW has been used in Ref. [32], which is sufficient to observe the above phenomena. However, the observation of noise-induced jumps between multistable states must include an additional noise source unless the current strength of the magnetostrictive interaction is increased by four orders of magnitude. Note that although the smaller YIG 2 gives a stronger magnomechanical coupling g compared to YIG 1, its corresponding magnon-microwave coupling g_{ma} however becomes weaker because it is proportional to the square root of the volume of the sphere. Our discussion uses a relatively weak magnon-microwave coupling $g_{ma} < 2\pi \times 4$ MHz, and both the YIG spheres can achieve this coupling since a very strong coupling $g_{ma} = 2\pi \times 143$ MHz has been realized for the YIG sphere with the diameter of 0.8 mm [5]. Furthermore, although the parameters we have chosen are not strict, we must emphasize that our method is general and the corresponding qualitative properties of the nonlinear dynamics do not depend on specific parameters.

Our analysis is based on one assumption that the mechanical mode exhibits single mode oscillatory rather than chaotic dynamics in a range with maximum rescale pump intensity $E = 0.05$, which corresponds to $B_0 = 34.4(68.0) \mu\text{T}$ and $P = 6.9(4.3)$ mW for YIG 1(2). By directly simulating the original Langevin equation (3) without any approximations, we find that chaotic behavior still does not appear even at $E = 30$ corresponding to $B_0 = 0.020(0.041)$ T and $P = 2.50(1.56)$ kW, which is an extremely large pump power [10]. Therefore, the formal solution (6) is a sufficiently universal hypothesis to analyze nonlinear phenomena in our model, while we will not discuss the situation where it is broken, unless the experimental conditions can support a significant increase in magnitude of the magnetostriction interaction.

In summary, we have explored the effect of nonlinear self-sustaining dynamics of cavity magnomechanics by generalizing the analysis corresponding to optomechanics via including the microwave-magnon beam splitter interaction. We have shown a multistability phase diagram by mapping out the attractors to the parameter space and have verified the analytical analysis numerically by applying stochastic Langevin equations. We have studied the influence of driving and microwave photon-magnon coupling on the

multistability. The fluctuation distribution of the system, for example, phase spread, amplitude compression, and the mixture of different limit cycles, is also shown by studying the corresponding Wigner functions. Finally, we have discussed the quantum-classical crossover of self-sustaining systems to demonstrate the efficient range of stochastic Langevin equations.

Our analytic derivation can free both theoretical and experimental researches of self-sustaining dynamics from time-consuming numerical simulations and provide a theoretical basis for applications related to limit cycles or multistability, such as phonon laser and weak signal detection. In addition, our paper can be generalized to multimode magnomechanics and transform the dynamic equations of multimechanical modes into Kuramoto types [44,67], which can provide a basis for studying quantum synchronization in cavity magnomechanics. It is worth noting that our derivation neglects the microwave and magnon mode perturbation by noise and the effect of these perturbations acting back on the mechanical mode due to the weak cooperativity [44,47]. Moreover, the restriction of the dimension of the Hilbert space can be extended by employing a method similar to the laser theory for optomechanics, which was proposed by Lörch

et al [63]. The related discussion would be an interesting subject for future investigations.

ACKNOWLEDGMENTS

W.L. is supported by the National Natural Science Foundation of China (Grant No. 12304389), by the Scientific Research Foundation of NEU (Grant No. 01270021920501*115), and in part by the European Union Horizon 2020 Programme for Research and Innovation through Project No. 732894 (FET Proactive HOT). J.C. is supported in part by the National Natural Science Foundation of China (Grants No. 11704205 and No. 12074206). W.-J. G. is supported in part by the Liao Ning Revitalization Talents Program (Grant No. XLYC1907033), the Natural Science Foundation of Liaoning province (Grant No. 2023-MS-072), the National Natural Science Foundation of China (Grant No. 11905027), and the Fundamental Research Funds for the Central Universities (Grants No. N2209005 and No. N2205015). J.L. is supported in part by the National Key Research and Development Program of China (Grant No. 2022YFA1405200) and National Natural Science Foundation of China (Grant No. 92265202).

-
- [1] C. Kittel, *Phys. Rev.* **73**, 155 (1948).
 - [2] H. Huebl, C. W. Zollitsch, J. Lotze, F. Hocke, M. Greifenstein, A. Marx, R. Gross, and S. T. B. Goennenwein, *Phys. Rev. Lett.* **111**, 127003 (2013).
 - [3] Y. Tabuchi, S. Ishino, T. Ishikawa, R. Yamazaki, K. Usami, and Y. Nakamura, *Phys. Rev. Lett.* **113**, 083603 (2014).
 - [4] X. Zhang, C. L. Zou, L. Jiang, and H. X. Tang, *Phys. Rev. Lett.* **113**, 156401 (2014).
 - [5] M. Goryachev, W. G. Farr, D. L. Creedon, Y. Fan, M. Kostylev, and M. E. Tobar, *Phys. Rev. Appl.* **2**, 054002 (2014).
 - [6] L. Bai, M. Harder, Y. P. Chen, X. Fan, J. Q. Xiao, and C. M. Hu, *Phys. Rev. Lett.* **114**, 227201 (2015).
 - [7] X. Zhang, C.-L. Zou, L. Jiang, and H. X. Tang, *Sci. Adv.* **2**, e1501286 (2016).
 - [8] C. A. Potts, E. Varga, V. A. S. V. Bittencourt, S. V. Kusminskiy, and J. P. Davis, *Phys. Rev. X* **11**, 031053 (2021).
 - [9] C. A. Potts, Y. Huang, V. A. S. V. Bittencourt, S. Viola Kusminskiy, and J. P. Davis, *Phys. Rev. B* **107**, L140405 (2023).
 - [10] J. Li, S. Y. Zhu, and G. S. Agarwal, *Phys. Rev. Lett.* **121**, 203601 (2018).
 - [11] M. Yu, H. Shen, and J. Li, *Phys. Rev. Lett.* **124**, 213604 (2020).
 - [12] B. Hussain, S. Qamar, and M. Irfan, *Phys. Rev. A* **105**, 063704 (2022).
 - [13] W. Qiu, X. Cheng, A. Chen, Y. Lan, and W. Nie, *Phys. Rev. A* **105**, 063718 (2022).
 - [14] C. Zhao, X. Li, S. Chao, R. Peng, C. Li, and L. Zhou, *Phys. Rev. A* **101**, 063838 (2020).
 - [15] H. Tan, *Phys. Rev. Res.* **1**, 033161 (2019).
 - [16] J. Li, S. Y. Zhu, and G. S. Agarwal, *Phys. Rev. A* **99**, 021801(R) (2019).
 - [17] H. Y. Yuan, P. Yan, S. Zheng, Q. Y. He, K. Xia, and M. H. Yung, *Phys. Rev. Lett.* **124**, 053602 (2020).
 - [18] S. F. Qi and J. Jing, *Phys. Rev. A* **105**, 022624 (2022).
 - [19] S. F. Qi and J. Jing, *Phys. Rev. A* **107**, 013702 (2023).
 - [20] A. Kani, B. Sarma, and J. Twamley, *Phys. Rev. Lett.* **128**, 013602 (2022).
 - [21] M. Asjad, J. Li, S.-Y. Zhu, and J. Q. You, *Fundam. Res.* **3**, 3 (2023).
 - [22] Q. Cai, J. Liao, B. Shen, G. Guo, and Q. Zhou, *Phys. Rev. A* **103**, 052419 (2021).
 - [23] S. F. Qi and J. Jing, *Phys. Rev. A* **103**, 043704 (2021).
 - [24] F. Y. Zhang, Q. C. Wu, and C. P. Yang, *Phys. Rev. A* **106**, 012609 (2022).
 - [25] S. N. Huai, Y. L. Liu, J. Zhang, L. Yang, and Y. X. Liu, *Phys. Rev. A* **99**, 043803 (2019).
 - [26] B. Wang, X. Jia, X. H. Lu, and H. Xiong, *Phys. Rev. A* **105**, 053705 (2022).
 - [27] D. Mukhopadhyay, J. M. P. Nair, and G. S. Agarwal, *Phys. Rev. B* **106**, 184426 (2022).
 - [28] Y. Zhou, S. Y. Xie, C. J. Zhu, and Y. P. Yang, *Phys. Rev. B* **106**, 224404 (2022).
 - [29] M. S. Ebrahimi, A. Motazedifard, and M. B. Harouni, *Phys. Rev. A* **103**, 062605 (2021).
 - [30] H. Y. Yuan, S. Zheng, Z. Ficek, Q. Y. He, and M. H. Yung, *Phys. Rev. B* **101**, 014419 (2020).
 - [31] Z. B. Yang, W. J. Wu, J. Li, Y. P. Wang, and J. Q. You, *Phys. Rev. A* **106**, 012419 (2022).
 - [32] R. C. Shen, J. Li, Z. Y. Fan, Y. P. Wang, and J. Q. You, *Phys. Rev. Lett.* **129**, 123601 (2022).
 - [33] A. Roulet and C. Bruder, *Phys. Rev. Lett.* **121**, 053601 (2018).
 - [34] G. Heinrich, M. Ludwig, J. Qian, B. Kubala, and F. Marquardt, *Phys. Rev. Lett.* **107**, 043603 (2011).
 - [35] J. Jin, D. Rossini, R. Fazio, M. Leib, and M. J. Hartmann, *Phys. Rev. Lett.* **110**, 163605 (2013).
 - [36] F. Iemini, A. Russomanno, J. Keeling, M. Schirò, M. Dalmonte, and R. Fazio, *Phys. Rev. Lett.* **121**, 035301 (2018).

- [37] P. Richerme, *Physics* **10**, 5 (2017).
- [38] A. Roulet and C. Bruder, *Phys. Rev. Lett.* **121**, 063601 (2018).
- [39] L. C. Kwek, *Physics* **11**, 75 (2018).
- [40] A. Mari, A. Farace, N. Didier, V. Giovannetti, and R. Fazio, *Phys. Rev. Lett.* **111**, 103605 (2013).
- [41] T. Weiss, A. Kronwald, and F. Marquardt, *New J. Phys.* **18**, 013043 (2016).
- [42] C. Navarrete-Benlloch, E. Roldán, and G. J. de Valcárcel, *Phys. Rev. Lett.* **100**, 203601 (2008).
- [43] C. Navarrete-Benlloch, T. Weiss, S. Walter, and G. J. de Valcárcel, *Phys. Rev. Lett.* **119**, 133601 (2017).
- [44] W. Li, P. Piergentili, J. Li, S. Zippilli, R. Natali, N. Malossi, G. Di Giuseppe, and D. Vitali, *Phys. Rev. A* **101**, 013802 (2020).
- [45] F. Marquardt, J. G. E. Harris, and S. M. Girvin, *Phys. Rev. Lett.* **96**, 103901 (2006).
- [46] T. E. Lee and H. R. Sadeghpour, *Phys. Rev. Lett.* **111**, 234101 (2013).
- [47] D. A. Rodrigues and A. D. Armour, *Phys. Rev. Lett.* **104**, 053601 (2010).
- [48] M. Aspelmeyer, T. J. Kippenberg, and F. Marquardt, *Rev. Mod. Phys.* **86**, 1391 (2014).
- [49] W. Li, W. Zhang, C. Li, and H. S. Song, *Phys. Rev. E* **96**, 012211 (2017).
- [50] V. Giovannetti and D. Vitali, *Phys. Rev. A* **63**, 023812 (2001).
- [51] H. J. Carmichael, *Statistical Methods in Quantum Optics* (Springer-Verlag, Berlin, 1999), Vol. 1.
- [52] W. Li, N. Es'haqi-Sani, W. Z. Zhang, and D. Vitali, *Phys. Rev. A* **103**, 043715 (2021).
- [53] G. Wang, L. Huang, Y. C. Lai, and C. Grebogi, *Phys. Rev. Lett.* **112**, 110406 (2014).
- [54] Note that this expression corresponds to the fixed-point iteration algorithm. Other iterative methods, such as nonlinear Newton iteration, can be used to accelerate convergence and expand the parameter range of convergence.
- [55] T. X. Lu, H. Zhang, Q. Zhang, and H. Jing, *Phys. Rev. A* **103**, 063708 (2021).
- [56] P. Piergentili, W. Li, R. Natali, N. Malossi, D. Vitali, and G. Di Giuseppe, *New J. Phys.* **23**, 073013 (2021).
- [57] Note that here the frequencies of the peaks are approximate but not strictly equal to $n\omega_b$ due to the slight dress effect of the mechanical mode. These slight dressings reflect the dynamic information of slowly varying amplitude A . At the same time, it was verified that there are several orders of magnitude differences between the time scale of the evolution of the slowly varying amplitude and the time scale of the sideband oscillations.
- [58] F. Bemani, Ali Motazedifard, R. Roknizadeh, M. H. Naderi, and D. Vitali, *Phys. Rev. A* **96**, 023805 (2017).
- [59] P. Piergentili, W. Li, R. Natali, D. Vitali, and G. Di Giuseppe, *Phys. Rev. Appl.* **15**, 034012 (2021).
- [60] I. Siddiqi, R. Vijay, F. Pierre, C. M. Wilson, M. Metcalfe, C. Rigetti, L. Frunzio, and M. H. Devoret, *Phys. Rev. Lett.* **93**, 207002 (2004).
- [61] R. M. Pettit, W. Ge, P. Kumar, D. R. Luntz-Martin, J. T. Schultz, L. P. Neukirch, M. Bhattacharya, and A. Nick Vamivakas, *Nat. Photon.* **13**, 402 (2019).
- [62] Z. Fu and L. Yang, *Phys. Rev. A* **105**, L061504 (2022).
- [63] N. Lörch, J. Qian, A. Clerk, F. Marquardt, and K. Hammerer, *Phys. Rev. X* **4**, 011015 (2014).
- [64] The magnitude of the term $\Omega^2/(\Delta^2 + \kappa^2)$ is approximately 10^{-4} in this case, leading to the magnitudes of the average number of photons corresponding to mode \hat{m} and mode \hat{a} of $\simeq 10^{-3}$ and $\simeq 10^{-4}$. Therefore, the 3×3 Hilbert subspace is enough for mode \hat{m} or \hat{a} .
- [65] L. Bakemeier, A. Alvermann, and H. Fehske, *Phys. Rev. Lett.* **114**, 013601 (2015).
- [66] J. Li and S. Gröblache, *Quantum Sci. Technol.* **6**, 024005 (2021).
- [67] C. A. Holmes, C. P. Meaney, and G. J. Milburn, *Phys. Rev. E* **85**, 066203 (2012).